Journal of Electron Spectroscopy and Related Phenomena 199 (2015) 10–18

Contents lists available at ScienceDirect

Journal of Electron Spectroscopy and Related Phenomena

journal homepage: www.elsevier.com/locate/elspec

Low-energy electron reflection from Au-passivated Ir(0 0 1) for application in imaging spin-filters

D. Vasilyev[a], C. Tusche[a], F. Giebels[b], H. Gollisch[b], R. Feder[a,b], J. Kirschner[a,c,*]

[a] Max-Planck-Institut für Mikrostrukturphysik, Weinberg 2, 06120 Halle, Germany
[b] Universität Duisburg-Essen, Fakultät für Physik, Campus Duisburg, Lotharstr. 1, 47048 Duisburg, Germany
[c] Martin-Luther-Universität Halle-Wittenberg, Institut für Physik, 06099 Halle, Germany

ARTICLE INFO

Article history:
Received 24 October 2014
Accepted 11 December 2014
Available online 19 December 2014

Keywords:
Condensed matter physics
Magnetism
Surface science

ABSTRACT

We describe the principle, the preparation, and the calibration of a spin-polarizing electron mirror in multichannel spin polarimetry. We show data obtained by two independent devices (a goniometer-type LEED set-up and a momentum-microscope set-up) and compare them to the results of a relativistic multiple scattering theory. We also discuss the effects of misalignment and mosaic structure of the crystal. For multi-channel detection we find a 5000-fold increase of efficiency over a single-channel spin-detector. The lifetime of the detector is more than 6 months in ultra-high vacuum.

1. Introduction

Electron spin polarimetry has recently been boosted by the introduction of the concept of multichannel spin analysis [1]. This means that the traditional one-channel spin detector has been replaced by an array of spin detectors (up to several thousands). This was accomplished by developing the "spin-polarizing electron mirror". In brief, this is a low energy electron diffraction set-up in which the incoming beam is composed of a multitude of small parallel beams diffracted from a spin selective single crystal surface in the specular geometry. Among the many diffracted beams the (0,0) beam is the only one which conserves the momentum parallel to the surface for elastic diffraction. After diffraction the individual beamlets are recombined by an electrostatic lens, and an image of the electron source distribution is generated on a multichannel detector. This two-dimensional distribution either can be the high-resolution spatial image of a photoelectron emission microscope [1], or the intensity distribution in the exit plane of an energy-dispersive analyzer [2], or the k-image of a momentum microscope (see below).

Since we make use of the spin-orbit interaction in the elementary scattering process at the surface, the spin-polarizing power of the electron mirror is equal to the intensity asymmetry upon reversal of the primary beam polarization. In this way the spin polarization distribution in the primary beam is translated into an intensity distribution at the channel plate detector. A key component in this device is the single crystal surface serving as the spin-polarizing mirror.

In Refs. [1] and [2] this surface was chosen as W(0 0 1). This system has the practical inconvenience that it requires frequent cleaning of the surface (cf. Refs. [3] and [4]).

As a system, which offers a longterm stability of at least several months, a pseudomorphic Au layer on Ir(0 0 1), has recently been explored [5], measuring and calculating intensity and asymmetry of the 00-beam for energies in the range between 15 and 95 eV and angles between 10° and 70°.

In these overview (E, Θ) landscapes a most promising region compatible with the geometry of the imaging spin filters was identified for energy 40 eV and polar angle of incidence 45° [5].

In the present paper, the surface system Au/Ir(0 0 1) is investigated in sufficient detail to qualify for practical application as an imaging spin filter. Our calculations revealed sharp surface resonance features in intensity and spin asymmetry, which are associated with the emergence thresholds of non-specular beams.

In the yet unexplored low-energy region around 10 eV, these resonances lead to a sharp transition from large positive to large negative spin asymmetry within an energy window of about 1 eV.

Experiments carried out with two different setups in the low- and the high-energy region yielded intensity and spin asymmetry results in good agreement with their theoretical counterparts.

Furthermore, we found for Au/Ir(0 0 1) a rather high effective surface Debye temperature, which entails a high efficiency also at room temperature. Spin-resolved photoelectron momentum

* Corresponding author at: Max-Planck-Institut für Mikrostrukturphysik, Weinberg 2, 06120 Halle, Germany. Tel.: +49 3455582655.
E-mail address: sekrki@mpi-halle.mpg.de (J. Kirschner).

http://dx.doi.org/10.1016/j.elspec.2014.12.006

distributions, which were obtained with the Au/Ir(0 0 1) spin filter at the low-energy working point, are presented.

2. Goniometer experimental setup

The measurements were made with two independent experimental devices. The first one is a goniometer-type LEED diffractometer. In Fig. 1 we show schematically the arrangement of the Ir(1 0 0) crystal as the scattering target in front of a spin-polarized electron source, and a channel plate detector with a series of collimating apertures (3 mm diameter). A Cylindrical Mirror-Analyzer (CMA) [6] is used for Auger analysis of the Au layer on the Ir(1 0 0), which is produced by depositing Au atoms from the evaporator [7]. The latter includes a monitor of the Au atom flux, by measuring a part of the positive ion flux generated by the electrons bombarding the crucible containing the Au. This flux monitor is calibrated against the quartz thickness monitor which can be positioned at the location of the target when it is retracted upwards, perpendicular to the paper plane. The spin-polarized source is of the photoemission type, described in detail in [8]. Measurements of the reflectivity and spin asymmetry of the target are done by ramping the primary voltage at the photocathode while ramping the retarding grid in the detector in parallel, so that only the quasi-elastically scattered electrons from the target are counted. The spin-polarization of the primary electrons is switched periodically between up and down with respect to the paper plane (identical with the scattering plane) by switching between right-polarized and left-polarized light from a laser diode (830 nm). The spin-sensitivity $S(\Theta, E)$ (also called Sherman function) as a function of scattering angle Θ and energy E is obtained from the measured asymmetry A (Θ, E) divided by the estimated source polarization P_0: $(S = A/P_0)$, for details see [5].

The target is an Ir crystal with (0 0 1) surface orientation, spark-eroded from the central part of a large ingot [9] with dimensions 13 mm × 16 mm, thickness 0.8 mm, polished on both sides. On one

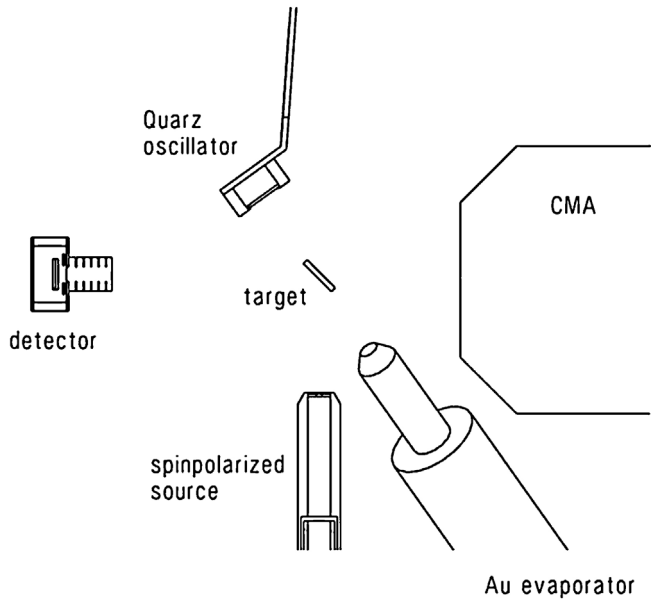

Fig. 1. Schematic view of the goniometer-type calibration set-up. The target (Ir(1 0 0)) is rotatable about the vertical axis (polar angle Θ). The pseudomorphic Au(1 × 1) monolayer is produced by Au deposition from the Au evaporator, which is calibrated by means of a quartz oscillator. The surface composition is determined by a CMA-type Auger analyzer. The primary spin-polarized electrons come from a strained layer photocathode. The electron detector consists of a double channel plate, preceded by a set of collimating apertures, which is rotatable about the target. The primary beam intensity is determined by the detector in the straight-through position after retracting the target and the quartz oscillator.

of the long sides a nose (2 mm × 3 mm) has been left over from the spark erosion which is held in a corresponding clamp. In this way a strain-free mounting of the crystal is achieved. For temperature measurements a W5%Re – W26%Re (Type C) thermocouple is inserted between the nose and the clamp. The azimuthal orientation is controlled by reflecting a laser beam from the short edge of the crystal to within ±0.5° with respect to the vertical rotation axis of the crystal manipulator.

The crystal and a part of its holder are heated by electron bombardment from the rear side up to 1700 K. The high voltage is positive with respect to ground and the filament is biased by +200 V. The easier way of putting the filament to negative high voltage is not recommended since the electrons cause electron stimulated desorption from the chamber walls during heating which deteriorates the vacuum to such an extent that it is impossible to obtain a clean crystal surface. The temperature measurement requires an isolated voltage amplifier [10].

The thermocouple reading has been cross-checked against an optical "disappearing-filament pyrometer" [11] aiming at the center of the crystal surface. It is found that the thermocouple reading is usually off the true temperature, by up to 20 K. This is to be expected since the thermocouple measures a temperature in between that of the crystal at the clamp and that of the clamp itself. This error is not too serious, though, since the crystal preparation procedure (see below) is not critically depending on the precise crystal temperature.

Our aim is to compare our experimental results to theoretical calculations. This requires a precise knowledge of the experimental scattering angles in our diffractometer-type apparatus. Since we have two independent rotation angles for target and detector we used two motor-driven vertical rotary feedthroughs with rotation axes perpendicular to the paper plane in Fig. 1. They are equipped with angular encoders with a resolution of less than 0.1°. Since the polar angle of the target is of primary importance, the proper zero angle has to be found. For this we made use of the properties of spin-orbit coupling in spin-polarized LEED which means here that for equivalent but opposite polar angles the diffracted intensities must be the same, while the asymmetries must be of opposite sign (assuming purely elastic scattering). The measured angular profiles are shown in Fig. 2 with an angular step size of 0.2°. The upper panel shows the intensities of the specular beam for two mirror-equivalent geometries: scattering to the left at a fixed angle of incidence of $\Theta = -10°$ with respect to the primary beam (blue) and $\Theta = +10°$, scattering to the right (red). The zero angle of incidence is found by slight variations of the target rotation until a satisfactory intensity symmetry is found. This defines the angular zero. The angular profile of the asymmetry is shown in the lower panel, displaying the expected antisymmetric behavior. The FWHM = 2.5° of the intensity profiles is primarily due to the detector resolution (calculated to be 1.8° from the distance detector-target and the aperture stack in front of the channel plates). This is proven by the saturation of the intensities and in particular the flat top of the asymmetry profiles. Taking the step edges of the profile into account we estimate an angular resolution of ±0.5° as given by the primary beam divergence.

Since intensity and asymmetry are both energy dependent a comment on the energetic profile of the primary beam is in order. As shown previously [6] the energy profile is determined by a high energy cut-off, (which is essentially constant with time) due to the photon energy and a low energy cut-off which shifts to higher energy with time after the preparation of the photocathode (due to the work function change). For an "aged" cathode we may assume a width of 150–300 meV. Since this is not explicitly resolvable in our retarding field analyzer in front of the detector we assume monoenergetic electrons accelerated to ground by the voltage applied to the photocathode plus a workfunction correction.

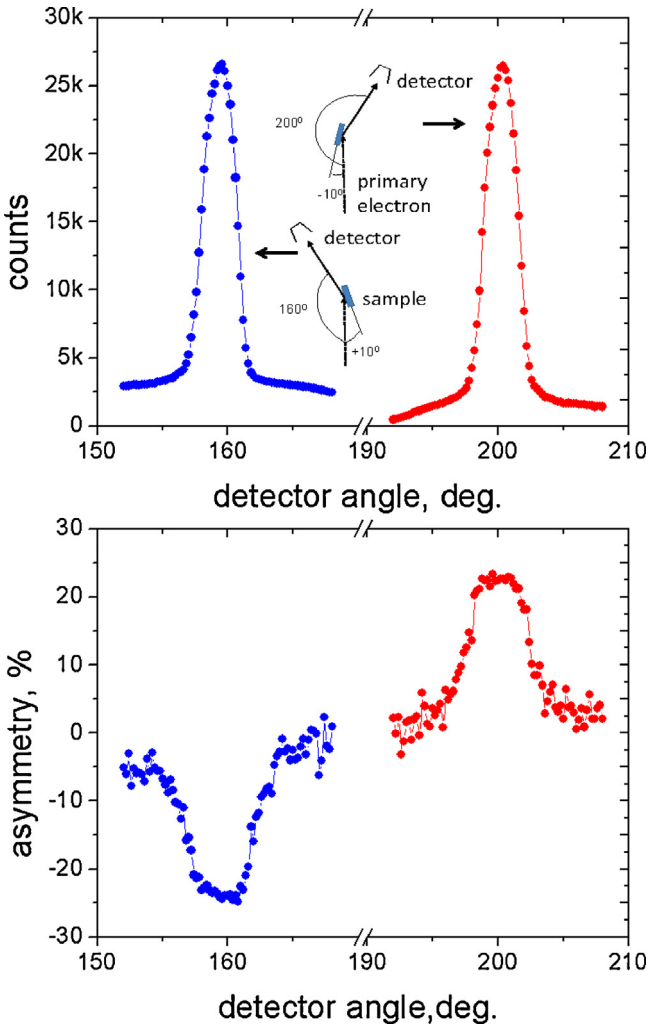

Fig. 2. Determination of the angle of incidence by two symmetric settings of the target and the detector. The precision is judged by the symmetry of the intensity angular scans (top) and the anti-symmetry of the asymmetry angular scans (bottom). The electron kinetic energy is 118 eV.

3. Momentum microscope experimental setup

Our goniometer-type setup provides good angular resolution and a narrow beam from the polarized electron source with fairly well-known spin-polarization. However, the relatively long travel paths and the magnetically difficult joining of two μmetal chambers make the measurements unreliable below about 20 eV. On the other hand, our theoretical results indicate an interesting plus–minus feature around 10 eV. Therefore, we employed another experiment, shown schematically in Fig. 3, which is based on a "momentum microscope" for photoemission [12]. It consists of a cathode lens, followed by an aberration-compensated hemispherical electron energy analyzer. The energy-filtered electrons are decelerated and focused onto the spin-polarizing mirror. Due to the compact design the magnetic shielding is much better and the device can operate down to 7 eV scattering energy at the mirror. We do not calibrate the detector by means of a separate electron source but employ an approximate "self calibration" using photoelectrons from the surface state of Au(1 1 1) excited by unpolarized light. It is well-known that the spin-polarization vectors within the spin-orbit split circular momentum distributions run along two circles in opposite sense, lying in the surface plane of the Au(1 1 1) crystal [13]. Fig. 4a shows the intensity and spin-polarization of the photoelectrons leaving the crystal with the component of the

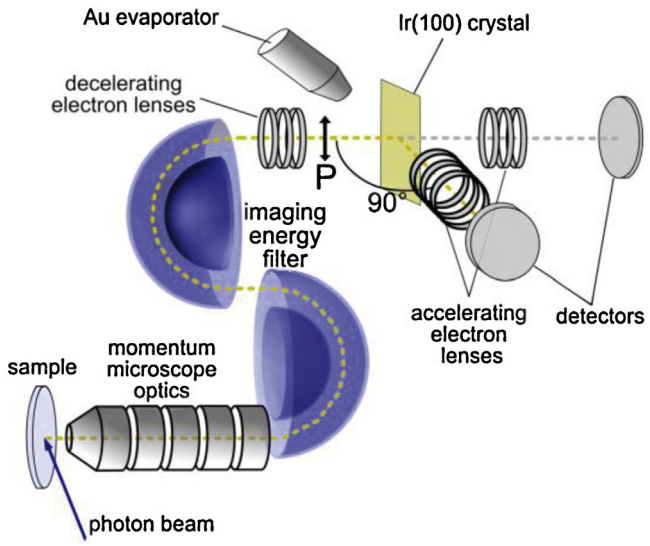

Fig. 3. Schematic view of the momentum microscope type set-up. Photoelectrons from a Au(1 1 1) sample ($h\nu = 21.5$ eV) are imaged and energy filtered (based on patent EP1.559.126 B1) and focused onto the Au(1 × 1)Ir(1 0 0) polarizing mirror. The momentum resolved intensities are analyzed by comparing the channel plate intensity patterns in the straight-through and the 90° positions.

polarization vector along the P-arrow in Fig. 3. This is the result after the analysis to be described below, where we employ a 2D color code for the intensity and the degree of polarization. Note that we see two circles of varying color and intensity. The colors are opposite in the left and the right halves and fade out in color along the vertical line at the middle. This indicates that the electrons with $K_x = 0$ have a vanishing spin-polarization projection along the P direction whereas the electrons with $K_y = 0$ have a maximum projection, changing sign when going from negative K_x to positive K_x. Note that the intensities are not equal on the left and right side due to off-normal incidence. These electrons are in general not 100% spin-polarized. In Ref. [13] the spin polarization is about 94–96% for p-polarized light under grazing incidence. Here we use unpolarized light, but contributions of s-polarization can be neglected (due to sp-character of SS). Therefore 100% polarization is assumed in the following.

Therefore the measured raw-intensity ratio cannot directly be used to calibrate the spin-polarizing mirror, but the primary photocurrent, before being reflected at the Au/Ir(1 0 0) mirror, has to be taken into account. A fairly good estimate can be made by including Fig. 4b and c. These display the intensity distribution after the polarizing mirror on the gray scale (black = high intensity, white = low intensity, according to the 2D color code above). We may then create a line profile in Fig. 4b along $K_y = 0$ with two double peaks. From left to right: a weak peak, a strong peak, a weak peak, a strong peak. We may decompose these doublets into two lines of a Voigt profile (a Lorentzian plus a Gaussian), independently on the left hand side and the right hand side. In this way we obtain four sets of partial intensities as a function of K_x. Next we introduce a scaling parameter S_v accounting for the spin sensitivity and multiply each two partial intensities by $1/(1 + S_v)$ and $1/(1 - S_v)$, respectively. We do the same for the other doublet with the same S_v and obtain four partial intensities. The sum of the absolute partial intensities must add up to the line profile we get for the measured intensity before the mirror, apart from a constant normalizing factor. If the fit is perfect, we found the desired polarization sensitivity $S = S_v$. If not, we repeat the fit procedures for a slightly different S_v and find better or worse agreement. The S value at the minimum of the residuum is our desired polarization sensitivity and the scatter gives us a measure of its accuracy. We do the same for Fig. 4c, at

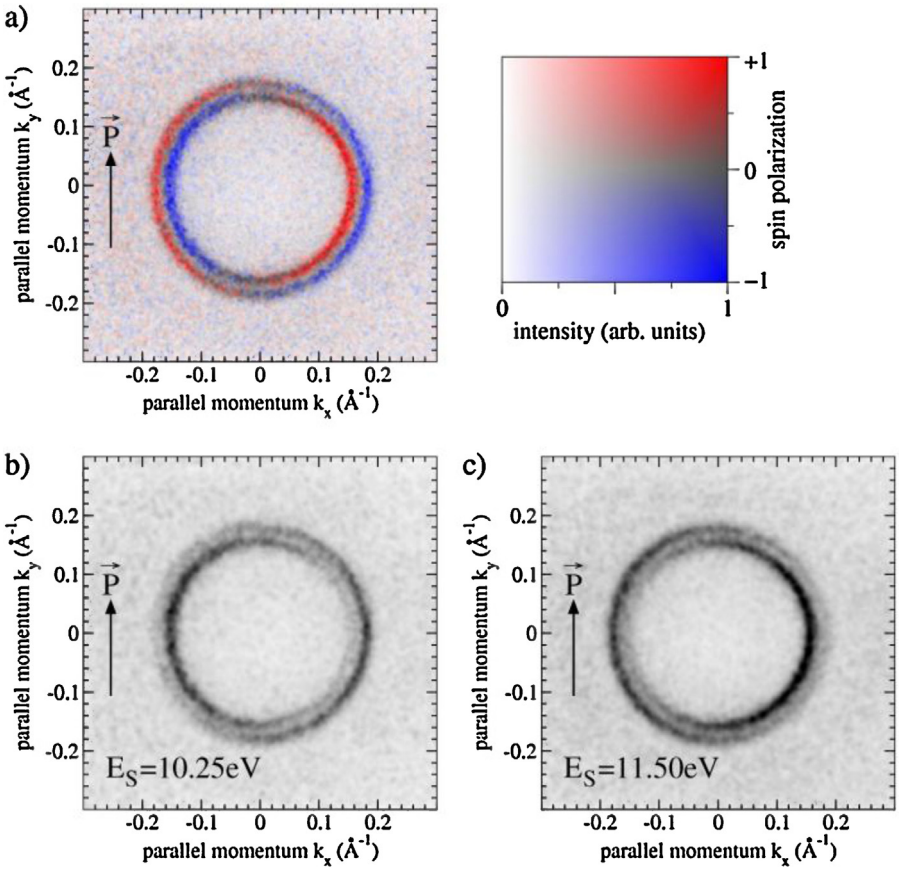

Fig. 4. (a) Parallel momentum distribution of the surface state of Au(1 1 1) after spin polarization analysis with respect to the vector indicated. Note the 2-dimensional color code for intensity and spin polarization. (b) Intensity distribution after the spin polarizing mirror at 10.25 eV scattering energy. (c) Intensity distribution at 11.50 eV scattering energy. Note the complementary black-and-white contrast in (b) and (c).

a different scattering energy and obtain the polarization sensitivity at that scattering energy. Repeating measurements and fitting for a range of energies E we finally obtain the energy dependence $S(E)$. This is shown in Fig. 11. The whole procedure is in the same spirit as outlined in [14] with the additional advantage that we may do the "self calibration" with a number of diagonals in Fig. 4, thus improving the accuracy.

4. Preparing the pseudomorphic Au(1 × 1) monolayer on Ir(1 0 0)

The key requisite for our polarizing mirror is a clean Ir(1 0 0) surface. While the usual adsorbates may be removed by a flash to 1200 °C, carbon persists. For this we adopted a procedure originally developed for tungsten [15], which works also for other refractory metals. It consists of cyclic heating to 1000 °C in an oxygen atmosphere ($0.5–3 \times 10^{-7}$ mbar). The adsorbed oxygen reacts with the surface carbon, forming CO, which may be monitored with a residual gas analyzer. In the cooling period carbon from the bulk segregates to the surface and is removed during the next heating period. In this way the surface and the near-surface bulk region is depleted of carbon. For a freshly cut and polished crystal it may take up to several days (cycling period 1–2 min), for a crystal with only surface contamination 15–20 min may suffice. The crystal is deemed clean, if no appreciable CO desorption occurs. At the end of this treatment the adsorbed oxygen is removed by a flash to

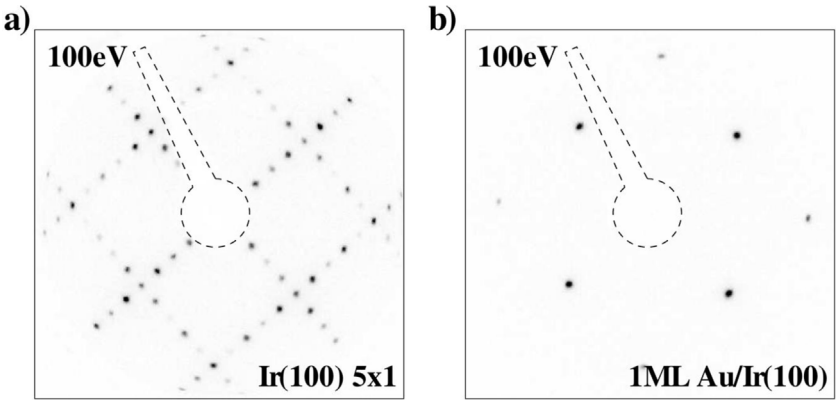

Fig. 5. (a) LEED pattern of the clean Ir(1 0 0)(5 × 1) crystal. (b) LEED patterns of the pseudomorphic Au(1 × 1) layer on Ir(1 0 0). Note that the superstructure has disappeared at 1 ML Au.

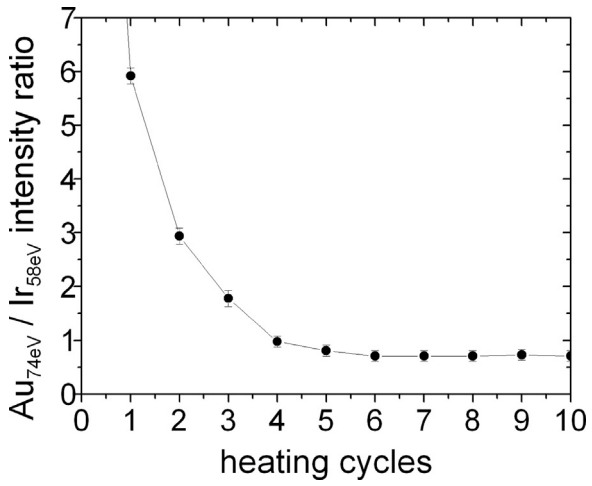

Fig. 6. Auger intensity ratio Au/Ir as a function of accumulated flashes to 860 °C. The initial decay indicates the desorption of Au multilayers. The flat portion corresponds to the pseudomorphic Au monolayer.

~1200 °C. This method is more sensitive than, e.g. Auger Spectroscopy.

Next, we deposit Au from the evaporator on the Ir(1 0 0) surface. After 1/4 to 1/3 of a monolayer Au, the Ir(5 × 1) reconstruction (see Fig. 5a) fades away, leaving a fuzzy (1 × 1) structure. Above 3 ML a new superstructure appears which superficially resembles the (5 × 1) reconstruction, but in fact it is not. Rather, it resembles that of the known c(28 × 48) reconstruction on Au(1 0 0) [16] which has been previously been identified as c(26 × 68). This indicates the presence of Au multilayers in two- or three-dimensional growth. Starting from a coverage of 2–3 ML the pseudomorphic monolayer is reached by a series of heating flashes (to 860 °C each, uncorrected thermocouple reading). Since this temperature is lower than the desorption temperature of the pseudomorphic monolayer, the Au multilayers are successively desorbed. This is demonstrated in Fig. 6 where the Auger peak-to-peak ratio is plotted as a function of the number of heating cycles. Obviously a constant level of the Au signal is reached after several cycles. The corresponding LEED pattern is seen in Fig. 5b, showing a (1 × 1) pattern without superstructures. This pattern is indistinguishable from the (1 × 1) pattern of the clean Ir(1 0 0). It was taken after heating cycle No. 8 in Fig. 6. The corresponding Auger spectrum in Fig. 7 may be taken as a reference for the pseudomorphic Au monolayer on Ir. This spectrum

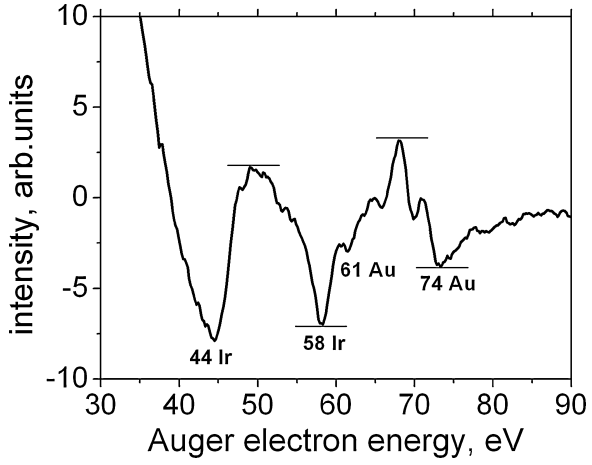

Fig. 7. Representative Auger spectrum for the pseudomorphic Au monolayer of Ir(1 0 0) with the peak-to-peak measurement positions indicated by the horizontal lines. The spectrum was taken after flash 8 in Fig. 6.

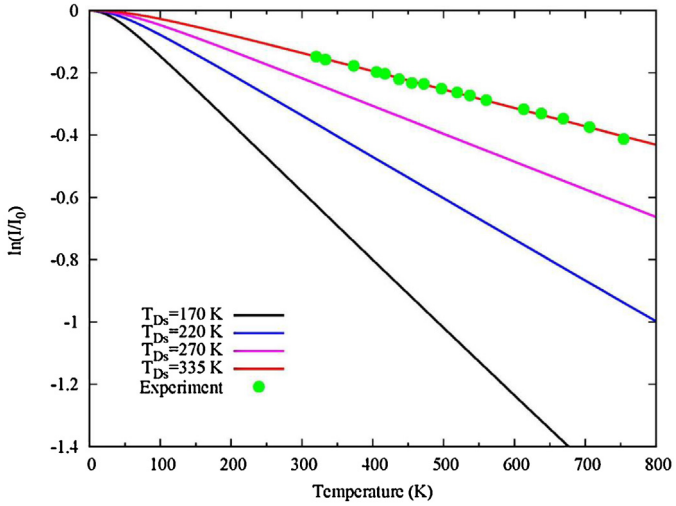

Fig. 8. Temperature dependence of the intensity of the LEED specular beam for primary beam energy 51.5 eV and polar angle of incidence 8° with azimuth along the [1 0 0] direction in the surface plane. Theoretical intensities Ith(T; T_{Ds}) for selected surface layer (Au) Debye temperatures T_{Ds} are represented as $ln[I^{th}(T; T_{Ds}) = I^{th}(T = 0K)]$ by the solid lines. The experimental intensities $I^{exp}(T)$ are shown as $ln[(I^{exp}(T) = I^{exp}(T = 320K))(I^{th}(T = 320K; T_{Ds}) = I^{th}(T = 0K)]$, i.e. the experimental data are shifted downward by the constant amount $ln[I^{th}(T = 320K; T_{Ds}) = I^{th}(T = 0K)]$ such that the lowest measured data point fits on the theoretical curve. For T_{Ds} = 335 K, all data points agree well with the theoretical curve, whereas for the other values of T_{Ds} they clearly deviate from the corresponding theoretical curves.

applies rigorously only to our CMA and our parameters (primary energy 3 kV, modulation amplitude 0.3 V, energy resolution 0.2 eV, normal beam incidence) but the relative peak heights are expected to be similar for any differentiated Auger spectrum, in particular the shape of the curve in Fig. 6.

With some experience and with a reasonably accurate temperature measurement at hand the preparation procedure can be shortened considerably: after deposition of 2–3 monolayers of Au, the crystal is annealed to 860 °C for about 2 min, including the initial heating. One or two of these annealings usually result in a pseudomorphic monolayer with the full polarization sensitivity. If this is not the case and the polarization sensitivity remains at 30–40% the cleaning procedure in oxygen should be repeated for several cycles. We attribute the reduced sensitivity to incomplete wetting of the Ir surface by Au, caused by submonolayer quantities of carbon.

5. Thermal lattice vibrations in SPLEED from Au/Ir(0 0 1)

Since thermal lattice vibrations reduce the LEED reflectivity with increasing temperature, they also affect the figure of merit of a spin detector. It is therefore important to assess their influence for our pseudomorphic Au–Ir(0 0 1) hybrid surface.

To this end, we measured, at fixed polar angle of incidence 8°, the height of a peak in the specular beam intensity as a function of temperature T in the range from 300 K to 750 K. In addition to Au–Ir(0 0 1), we did this also for the clean Ir(0 0 1) surface and a thick Au film on Ir(0 0 1).

As is well known ([17] and references therein), a straightforward way to evaluate such $I(T)$ curves is to assume an intensity decrease described by a Debye–Waller factor. From the slope of a linear fit to ln[$I(T)$] one then gets an effective Debye temperature T_D^{eff}. We thus obtained the values 260 K, 274 K and 130 K for 1 ML Au on Ir, clean Ir(0 0 1) and thick Au on Ir, respectively. The effective Debye temperature of 1 ML Au on Ir is thus very close to the one of Ir(0 0 1) and twice as large as the one for thick Au on Ir(0 0 1). For comparison, we note that the bulk Debye temperature of Ir is much higher (430 K) than the one for Au (170 K) [18].

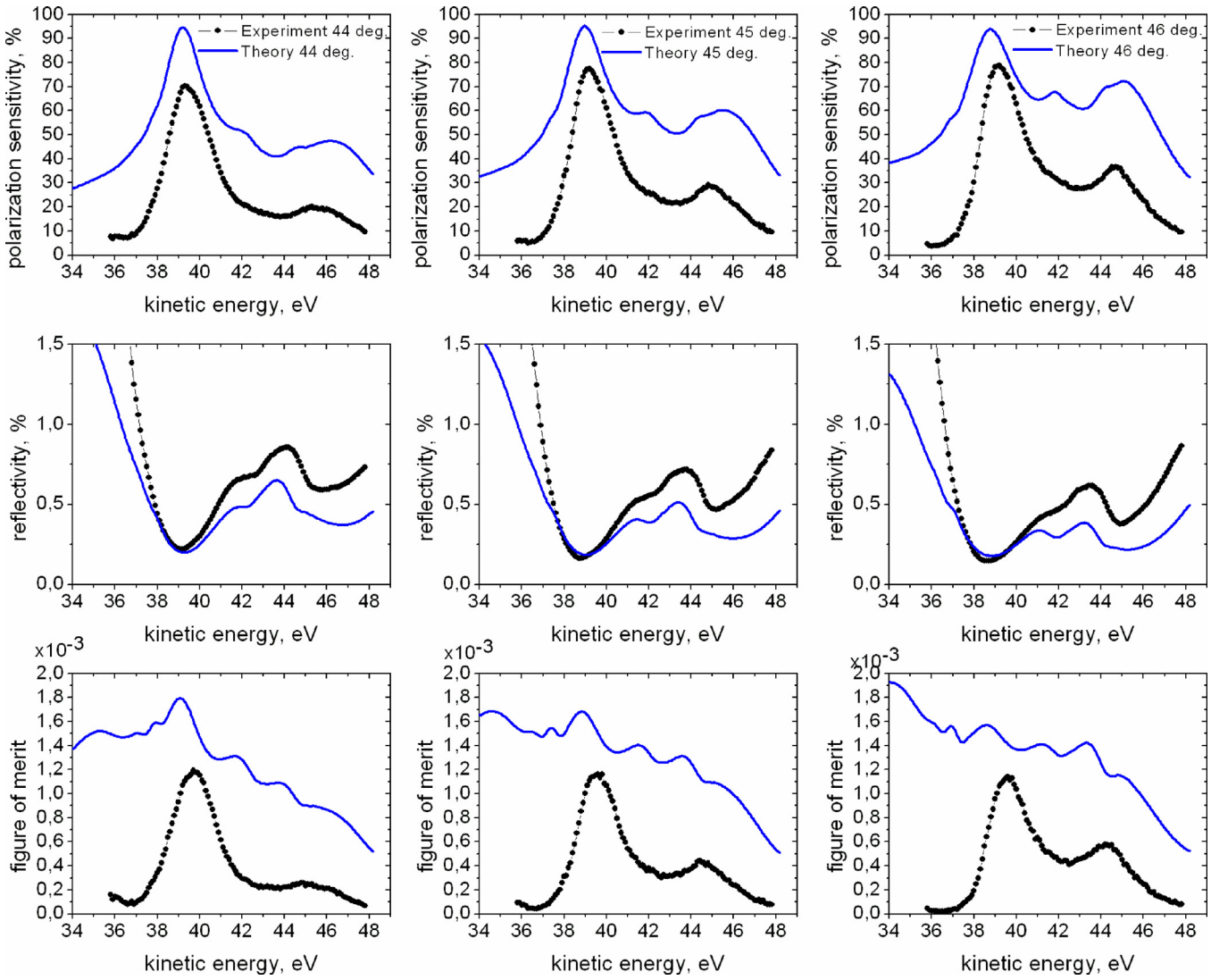

Fig. 9. Comparison of experimental (black dots) and theoretical data (blue lines) for the polarization sensitivity (top row), the reflectivity (center row) and the figure of merit (bottom row) for polar angle of indicidence 44° (left), 45° (center), and 46° (right). Note that no scaling factors have been applied. The experimental polarization data have been obtained by means of the spinpolarized electron source.

Assuming an intensity decrease with a Debye–Waller factor, one neglects however elastic multiple scattering, which plays an important role in LEED. A more appropriate procedure for extracting information from our measured $I(T)$ curves is to compare them with their theoretical counterparts calculated by means of a relativistic multiple scattering formalism ([19] chapter 4) in which thermal lattice vibration effects are taken into account via layer-dependent Debye temperatures. While the Debye temperature in the deeper layers has the known bulk value, its values in the near surface layers have to be treated as parameters to be determined via comparison with experiment [20]. For 1 ML Au on Ir we chose, as an approximation, the Ir bulk value 430 K for all Ir layers and kept the Debye temperature for the Au layer as a parameter T_{Ds}, with the subscript '*s*' indicating 'surface layer'.

Theoretical intensity versus temperature results $I^{th}(T)$ for selected values of T_{Ds} are shown in Fig. 8 as $ln[I^{th}(T)/I^{th}(T=0)]$ together with our experimental results for 1 ML Au/Ir(1 0 0). Above about 150 K, all calculated curves exhibit an almost linear decline with increasing temperature. This decline is strongest for T_{Ds} = 170 K, which corresponds to the bulk Debye temperature of Au, and decreases with increasing T_{Ds}. For T_{Ds} = 335 K, very good agreement is reached with our experimental data.

For the surface layer of clean Ir, we obtained T_{Ds} = 340 K, which is somewhat higher than for the Au monolayer. This is qualitatively in line with the relation between the above effective Debye temperatures.

The Debye temperature value of 335 K was subsequently used in calculations of SPLEED intensity and asymmetry curves from 1 ML Au on Ir as functions of energy and polar angle of incidence.

Our finding that the Debye temperatures (effective, surface and bulk) for 1 ML Au on Ir are much larger than those for thick Au has an important implication for spin detectors, which usually operate at room temperature. While at T = 0 both surface systems are likely to produce LEED intensities of similar magnitude, at room temperature the intensity from 1 ML Au on Ir is significantly higher than from clean Au. This is an additional advantage for a spin detector based on a pseudomorphic monolayer of Au on Ir.

6. Spin polarization sensitivity, reflectivity and figure of merit

We distinguish between the "high energy region" around 39 eV (Figs. 9 and 10) and the "low-energy region" around 11 eV (Fig. 11). Fig. 9 shows a compilation of our experimental (black) and

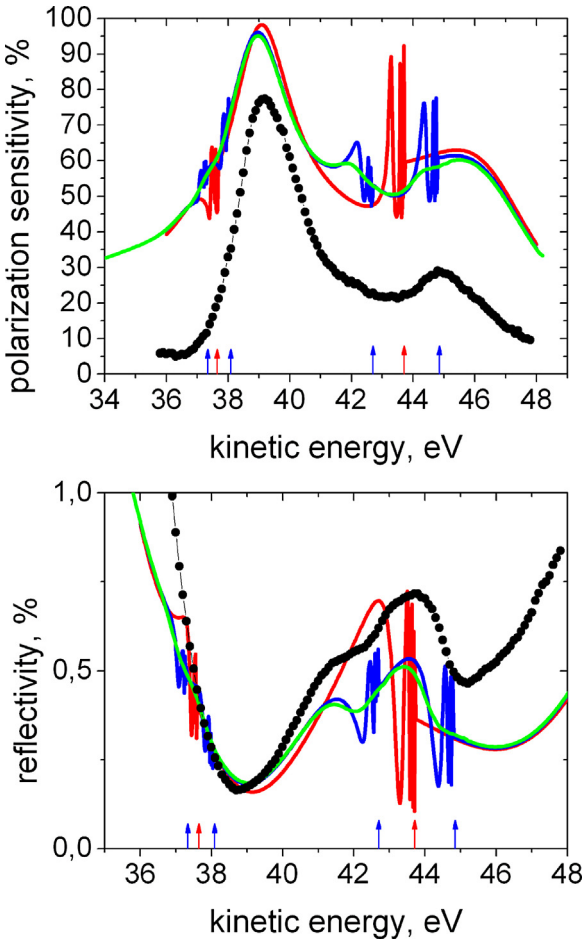

Fig. 10. Polarization sensitivity (top) and intensity (bottom) as a function of kinetic energy for the specular beam at $\Theta = 45^\circ$. Black dots: experiment, red line: theory for azimuthal scattering angle $\varphi = 0^\circ$. Blue line: theory for $\varphi = 1.2^\circ$. Green line: theory for $\varphi = 1.2^\circ$ after convolution with a Gaussian function. Details see text. The vertical arrows indicate emergence thresholds for non-specular beams.

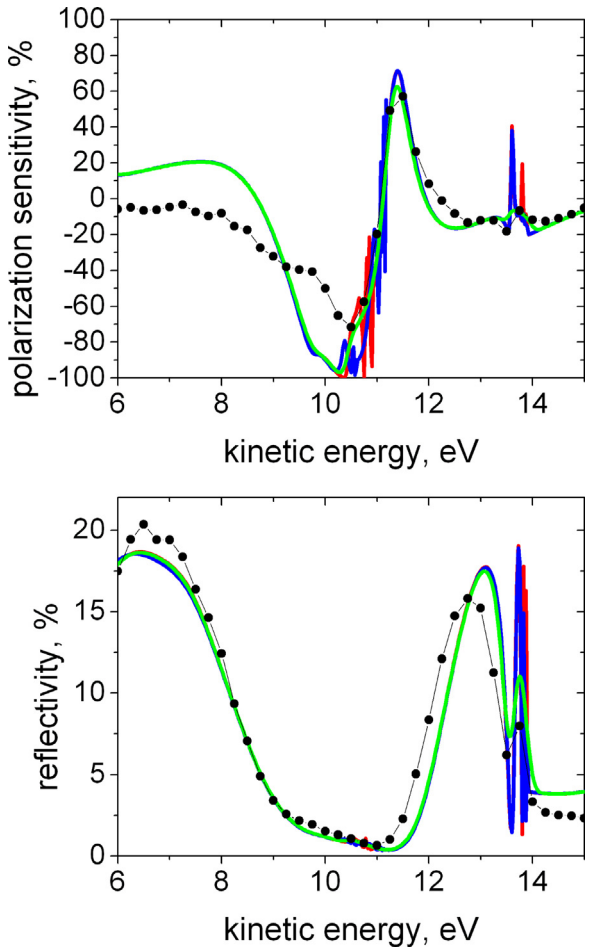

Fig. 11. Polarization sensitivity (top panel) and intensity (bottom panel) in the low energy region as a function of kinetic energy for polar angle $\Theta = 0^\circ$. The experimental data (black dots) have been obtained by our "self-calibration" procedure. Red lines: theory, azimuthal angle $\varphi = 0^\circ$. Blue lines: theory, $\varphi = 1.2^\circ$. Green lines: theory for $\Theta = 45^\circ$ and $\varphi = 0^\circ$ with threefold Gaussian convolution. Details see text.

theoretical (blue) data for polarization sensitivity (top row), reflectivity (middle row), and figure of merit (bottom row). The experimental polarization sensitivity has been obtained through the calibration with our primary source, for which a spin polarization of $P_0 = 80\%$ was used, based on the arguments in [5] with the light polarization of 0.92 and the intrinsic polarization of 0.86 of the photoelectrons generated in the photocathode. We observe a high polarization sensitivity of 70–80%. Note that here, as well as in the other plots, we display our experimental and theoretical results on the same scales without any scaling factors.

The reflectivity in the center panel was determined by normalizing the count rate in the specular beam to the count rate in the primary beam when we place our detector in the straight-through position. In this way the unknown detection probability of the channel plates cancels out. Near 39 eV we observe the usual "rule of thumb" namely that a polarization maximum is associated with an intensity minimum. This is not a "law", though, since a local intensity maximum may be associated with sizeable asymmetry (see, e.g. near 43 eV). This effect is due to multiple scattering in the target.

When we compare experiment and theory we have to keep in mind that we do not strictly compare the same quantities: the theory describes strictly elastic scattering of strictly monochromatic electrons. In the experiment we measure "quasielastically" scattered electrons within a certain energy distribution within a certain energy window. Our source has a distribution about 0.1–0.3 eV wide and we admit an energy window of 2–3 eV width in our retarding field analyzer. We could make this window narrower but since we think of a spin detector we need both, asymmetry and intensity. One has to find a compromise since the acceptance of inelastically scattered electrons inevitably causes a loss of the primary polarization. This is due to exchange interaction: a primary electron kicks out an electron from the valence band, thus its spin is not directly related to that of the incoming electron. In paramagnets the net polarization is thus reduced. The larger the energy loss, the larger the depolarization and the larger the momentum change [21]. The presence of weakly polarized and unpolarized electrons within the detector window may lead to surprisingly large depolarization effects (see the model calculations in [22]. Our observation of incomplete polarization sensitivity and somewhat enhanced reflectivity may then be partly due to inelastic scattering.

In ferromagnets this process may even enhance the polarization sensitivity as in the spin detector using epitaxial Fe [23], though at the expense of momentum conservation. This process is often erroneously called "spin flip scattering" though no electron flips its spin.

The figure of merit is a measure of the time it needs in an actual measurement to reach a given statistical uncertainty per pixel. It is proportional to the expression $f(E) = S^2(E)^*R(E)$, with polarization sensitivity, S, and reflectivity, R, at energy E. This is plotted in the bottom row of Fig. 9 for the experimental data (black dots) and the theoretical results (blue line). We find that experimentally

there is a maximum near 40 eV for all the angles considered. Somewhat surprisingly it is nearly constant as a function of polar angle at $f = 1.2 \times 10^{-3}$ because the slight increase of the asymmetry from $\Theta = 44^\circ$ to $\Theta = 46^\circ$ is compensated by a decrease of reflectivity over the same range. This is clearly beneficial for the operation of the spin-detector at $\Theta = 45^\circ \pm 1^\circ$. For the analysis of a 2D distribution of intensity and spin polarization over a range of energies one has to do a pixel-by-pixel calculation taking the data for polarization sensitivity and reflectivity into account for each energy [1,2]. The useful range of energies is about 3 eV around the peak of the figure of merit if one accepts a variation of about a factor of two of the figure of merit.

7. Surface barrier resonances

The most sensitive response of the diffracted intensity with respect to electron momentum occurs at surface barrier resonances, i.e. when a diffracted beam travels nearly parallel to the surface. The crossing of this condition for a small change of the parallel momentum of the primary electrons leads to rapid oscillations of the diffracted intensity detected outside of the crystal. This is seen in Fig. 10 where the momentum varies with the electron energy at constant angles. See the red lines in the top and bottom panels. The oscillations resemble a Rydberg series, converging to the escape threshold of a beam, marked by the arrows at the bottom lines. These oscillations occur in both the reflectivity and the polarization sensitivity [26]. We observe them near two energies (around 37.7 eV and 43.8 eV). This is explained by the strong multiple scattering in low energy electron diffraction: what happens to one beam is felt by all other beams, even if they are far from the surface resonance condition. This is also demonstrated by the blue lines, where an azimuthal rotation of 1.2° has been assumed. Now we see the splitting of the resonance feature in the red lines into two, shifted to higher and lower energy by about the same amount. Because of the slight misorientation we have now two thresholds (see the blue arrows) one for a smaller wavevector and one for the larger wavevector, hence the double resonance features.

In a real crystal we may have a large number of mosaic blocks each with a different misorientation of the azimuthal angle, with a certain distribution function over the surface area illuminated by the primary beam.

The influence of a mosaic structure of the scattering crystal on polarization sensitivity and reflectivity has not been treated before. We will discuss some of the pertinent aspects semiquantitatively, but we cannot perform a full study since we do not know the mosaic structure of our crystal in detail and cannot measure it at the present development stage of spin-polarized LEED diffractometry. A nominally single crystalline sample contains a large number of mosaic blocks which may be misoriented with respect to polar and azimuthal angles [24,25]. The degree of disorder and the distribution functions are not known, but the amount of misalignment may be of the order of 0.1° to ≈1.5° for a metal single-crystal, depending on the material and the growth conditions. The mosaic structure is not homogeneous across the crystal, not even isotropic. The size of the mosaic blocks may be of the order of ∼100 lattice constants, i.e. large relative to the mean free path of low energy electrons. Therefore, a diffraction pattern may be obtained form the incoherent superposition over many mosaic blocks.

To account for this effect, the spin dependent intensities $I^\sigma(E, \Theta, \varphi)$ were calculated on a mesh with $\delta E = 0.025$ ev, $\delta\Theta = 0.1^\circ$ and $\delta\varphi = 0.2^\circ$.

For fixed angles Θ and φ, intensities $I^\sigma(E)$ were then obtained by convoluting the intensities $I^\sigma(E, \Theta, \varphi)$ with a threefold Gaussian of the form $exp(-E^2/g_E{}^2)exp(-\Theta^2/g_\Theta{}^2)exp(\varphi^2/g_\varphi{}^2)$, with the halfwidth parameters g_E, g_Θ and g_φ chosen as 0.1 eV, 0.5° and 0.5°, respectively.

Finally, spin-averaged intensity and polarization sensitivity spectra were calculated from the intensities $I^\sigma(E)$.

The result is shown by the green curves in Fig. 10. Obviously the fine structure does not average out but give rise to new structures on the eV scale for both asymmetry and intensity. We applied this procedure for all theoretical data in the top and middle row of Fig. 9 and found that the agreement between theory and experiment is improved. The lesson we learn is that nominally identical crystals may not yield exactly the same experimental results because of the mosaic structure. If high demands are set on the precision of the spin polarization analyzers each crystal will require its own calibration curves.

We also applied the above procedure in the low energy region, see Fig. 11. For $\Theta = 45.5^\circ$ and $\varphi = 0$, the energy range below 15 eV comprises two emergence thresholds of non-specular beams, one at 10.90 eV and the other at 13.89 eV. Below each of them, the "sharp" theoretical spectra (calculated for fixed Θ and φ on a fine (0.025 eV) energy mesh) exhibit a series of surface barrier resonances.

Going to non-zero φ (in particular to $\varphi = 1.2^\circ$ as shown in Fig. 11 the two thresholds and consequently the two surface resonance behave differently.

At the 10.90 eV threshold for $\varphi = 0$, two non-specular beams emerge, which are symmetric with respect to the $\varphi = 0$ mirror plane. For non-zero φ, these two beams emerge at two different energies, i.e. there are now two series of surface resonances. At the 13.89 eV threshold for $\varphi = 0$, however, there emerges only one non-specular beam. For non-zero φ, one then has only one emergence threshold, at a slightly lower energy. We note that the variation of polarization sensitivity and intensity happens on a much finer scale (step size 0.25 eV) and that there is a pronounced plus/minus feature of the polarization with the extrema only ∼1 eV apart on the energy scale. This means that the useful energy range is restricted to about 0.1 eV and that a wide energy beam could not be analyzed without scanning the energy. For a monochromatic image, such as in our momentum microscope, this bears a definite advantage because with two measurements (one on the negative extreme and one on the positive one) the apparatus asymmetry can efficiently be eliminated [27]. The polarization sensitivity has been determined with our "self-calibration" described above. The scatter of the data points in the flat portions (6–8 eV and 14–15 eV) give a hint of the reproducibility of the calibration.

As far as the figure of merit is concerned, we note that the reflectivity in this range is much higher than in the high energy range, even near its minimum where the asymmetry extrema are located. With reference to Fig. 4, where the two relevant scattering energies are given, at 10.25 eV we measure a reflectivity of 1.29%, and at 11.50 eV of 2.26%. With a polarization sensitivity of −65% at 10.25 eV and 57% at 11.50 eV we obtain a figure of merit of 5.48×10^{-3} and 7.38×10^{-3} respectively.

8. Application of the spin-polarizing mirror in 2-dimensional multichannel spin-polarimeters

Suppose we have a surface emitting electrons (e.g. secondary electrons, or inelastically scattered electrons, or photoelectrons) into the half-space above the surface with a certain transverse spin orientation parallel to the surface. Conventionally, one uses an energy analyzer followed by a spin detector and scans the angular distribution. This is time consuming and asks for multichannel detection. To be specific we assume the system sketched schematically in Fig. 3, which consists of an imaging lens system, followed by an imaging energy filter, followed by the spin-polarizing mirror. In this section we wish to discuss the question "how many channels can we use simultaneously and what is the gain over a conventional single channel system?"

An important quantity characterizing a single channel spin detector is the figure of merit f. It is a small number ($f = 10^{-4} \ldots 10^{-2}$) depending primarily on the type of detector employed. For multichannel detectors we have recently defined a 2-dimensional figure of merit $F_{2D} = N{\cdot}f$ where N is the number of channels available. N can be large (of order 10^2–10^4) depending primarily on the electron-optical design. Thus f characterizes mainly the type of detector while F_{2D} characterizes mainly the device as a whole. F_{2D} may be of order 10.

The number of channels in our above example is given by the broading in $K_{||}$ space introduced by the scattering at the detector crystal. With the Gaussian part of the Voigt-function discussed above we estimate that we can resolve about $80 \times 80 = 6400$ pixels which reduces to $N = 5000$ because we have circular channel plates. With the figure of merit quoted above at the working point $E = 10.25$ eV we arrive at a two-dimensional figure of merit $F_{2D} = 37$. This means that we can analyze the same region of $K_{||}$ space about 5000 times faster than with a single channel detector with the same energy- and k-space resolution and the same value of f. This demonstrates the enormous gain in efficiency that can be obtained by multichannel detection with the spin-polarizing mirror.

Acknowledgement

We thank H. Engelhard, R. Neumann, H. Menge, F. Thiele and D. Hartung for their expert technical help.

References

[1] C. Tusche, M. Ellguth, A.A. Ünal, C.-T. Chiang, A. Winkelmann, A. Krasyuk, M. Hahn, G. Schönhense, J. Kirschner, Spin resolved photoelectron microscopy using a two-dimensional spin-polarizing electron mirror, Appl. Phys. Lett. 99 (2011) 032505.
[2] M. Kolbe, P. Lushchyk, B. Petereit, H.J. Elmers, G. Schönhense, A. Oelsner, C. Tusche, J. Kirschner, Highly efficient multichannel spin-polarization detection, Phys. Rev. Lett. 107 (2011) 207601.
[3] D. Yu, C. Math, M. Meier, M. Escher, G. Rangelov, M. Donath, Characterization and application of a SPLEED-based spin polarization analyzer, Surf. Sci. 601 (2007) 5803.
[4] F. Lofink, S. Hankemeier, R. Frömter, J. Kirschner, H.P. Oepen, Long-time stability of a low-energy electron diffraction spin polarization analyzer for magnetic imaging, Rev. Sci. Instrum. 83 (2012) 023708.
[5] J. Kirschner, F. Giebels, H. Gollisch, R. Feder, Spin-polarized electron scattering from pseudomorphic Au on Ir(0 0 1), Phys. Rev. B 88 (2013) 125419.
[6] DESA 100, Staib Instruments, sales@staibinstruments.com, phone: +49-8761-76240.
[7] J. Kirschner, H. Engelhard, D. Hartung, An evaporation source for ion beam assisted deposition in ultrahigh vacuum, Rev. Sci. Instrum. 73 (2002) 3853.
[8] J. Kirschner, H.P. Oepen, H. Ibach, Energy- and spin-analysis of polarized photoelectrons from NEA GaAsP, Appl. Phys. A 30 (1983) 177.
[9] MaTeck GmbH, Im langen Broich 20, 52428 Juelich, Germany, www.mateck.de
[10] type SINEAX V624, Camille Bauer Metrawatt AG, Aargauerstr. 7, CH-5610 Wohlen AG, Switzerland, www.camillebauer.com
[11] Portable Pyrometer Mikro PV11, Keller HCW GmbH, Division MSR, Carl-Keller-Str. 2–10, 49479 Ibbenbüren, Germany, www.keller-mrs.com
[12] B. Krömker, M. Escher, D. Funnemann, D. Hartung, H. Engelhard, J. Kirschner, Development of a momentum microscope for time resolved band structure imaging, Rev. Sci. Instrum. 79 (2008) 053702.
[13] J. Henk, A. Ernst, P. Bruno, Spin polarization of the L-gap surface states on Au(1 1 1), Phys. Rev. B 68 (2003) 165416.
[14] F. Meier, H. Dil, J. Lobo-Checa, L. Patthey, J. Osterwalder, Quantitative vectorial spin analysis in angle-resolved photoemission: Bi/Ag(1 1 1) and Pb/Ag(1 1 1), Phys. Rev. B 77 (2008) 165431.
[15] Kh. Zakeri, T.R.F. Peixoto, Y. Zhang, J. Prokop, J. Kirschner, On the preparation of clean tungsten single crystals, Surf. Sci. 604 (2010) L1.
[16] (a) R. Hammer, A. Sander, S. Förster, M. Kiel, K. Meinel, W. Widdra, Surface reconstruction of Au(0 0 1): high-resolution real-space and reciprocal-space inspection, Phys. Rev. B 90 (2014) 035446;
(b) M.A. van Hove, R.J. Koestner, P.C. Stair, J.P. Bibérian, L.L. Kesmodel, I. Bartôs, G.A. Somorjai, The surface reconstructions of the (1 0 0) crystal faces of iridium, platinum and gold I. Experimental observations and possible structural models, Surf. Sci. 103 (1981) 189.
[17] J.B. Pendry, Low Energy Electron Diffraction: The Theory and Its Application to Determination of Surface Structure, Academic Press, USA, 1974, ISBN 978-0-12-550550-5.
[18] Debye Temperature of Ir, Au, www.infoplease.com/periodictable
[19] R. Feder, Polarized Electrons in Surface Physics, World Scientific Publishing Co. Pte. Ltd., Singapore, 1985.
[20] W. Hösler, W. Moritz, E. Tamura, R. Feder, Influence of the scattering potential model on low energy electron diffraction from Cu(0 0 1)–c(2 × 2)–Pb, Surf. Sci. 171 (1986) 55.
[21] H. Hsu, M. Magugumela, B.E. Johnson, F.B. Dunning, G.K. Walters, Use of spin-polarized electron-energy-loss spectroscopy to investigate dipole and impact scattering from transition-metal surfaces, Phys. Rev. B 55 (1997) 13972.
[22] Note that according to the definition of the degree of spin polarization $p = N\uparrow - N\downarrow / N\uparrow + N\downarrow$ the polarization is a strongly non-linear function of the ratio $N\uparrow/N\downarrow$. E.g. for a ratio of 2 one finds $P2 = 33\%$, whereas for a ratio of 10 one obtains $P10 = 10 - 1/10 + 1 = 82\%$. This means that even for a small admixture of unpolarized electrons the effective polarization is drastically reduced. Assume that we have a 10% unpolarized background flux in the minority channel of the above example. Then we find a polarization of $\tilde{P} = 10 - (1+1)/10 + (1+1) = 66\%$.
[23] A. Winkelmann, D. Hartung, H. Engelhard, C.-T. Chiang, J. Kirschner, High efficiency electron spin polarization analyzer based on exchange scattering at Fe/W(0 0 1), Rev. Sci. Instrum. 79 (2008) 083303.
[24] H. Wenzl, H. Schlich, Crystals and crystal growth – an introductory survey, www.mateck.de
[25] C.G. Darwin, The reflexion of X-rays from imperfect crystals, Phil. Mag. 43 (257) (1922) 800 (Special issue 6th series).
[26] D.T. Pierce, R.J. Celotta, G.-C. Wang, E.G. McRae, Spin dependence of electronic surface resonance scattering from W(1 0 0), Solid State Commun. 39 (1981) 1053.
[27] C. Tusche, M. Ellguth, A. Krasyuk, A. Winkelmann, D. Kutnyakhov, P. Lushchyk, K. Medjanik, G. Schönhense, J. Kirschner, Quantitative spin polarization analysis in photoelectron emission microscopy with an imaging spin filter, Ultramicroscopy 130 (2013) 70.